*Manuscript
Click here to view linked References

©2016. This manuscript version is made available under the CC-BY-NC-ND 4.0 license http://creativecommons.org/licenses/by-nc-nd/4.0/
This is the accepted version of the manuscript published in Materials & Design at https://doi.org/10.1016/j.matdes.2016.11.106

# Exceptional thermal strain reduction by a tilting pillar architecture: suspended Ge layers on Si (001)

*Anna Marzegalli[a], Andrea Cortinovis[a], Francesco Basso Basset[a], Emiliano Bonera[a], Fabio Pezzoli[a], Andrea Scaccabarozzi[a], Fabio Isa[b], Giovanni Isella[c], Peter Zaumseil[d], Giovanni Capellini[d e], Thomas Schroeder[d], Leo Miglio[a,]**

[a]L-NESS and Department of Materials Science, Università di Milano-Bicocca, via Cozzi 55, I-20125, Milano, Italy

[b]Laboratory for Solid State Physics, ETH Zürich Schafmattstr. 16, CH-8093 Zürich, Switzerland

[c]L-NESS and Department of Physics, Politecnico di Milano, via Anzani 42, I-22100, Como, Italy

[d]IHP, Im Technologiepark 25, 15236 Frankfurt (Oder), Germany

[e]Department of Science, Università Roma Tre, Viale Marconi 446, 00146 Roma, Italy

* corresponding author. E-mail address: leo.miglio@unimib.it. Phone: +39 02 6448 5217

In this paper we present the exceptional thermal strain release provided by micrometric Si pillar arrays to Ge epitaxial patches suspended on them, for different pillar aspect ratios and patch sizes. By combining 3D and 2D Finite Element Method simulations, low-energy plasma-enhanced chemical vapour deposition on patterned Si substrates, μ-Raman, μ-photoluminescence and XRD measurements, we provide a quantitative and consistent picture of this effect with the patch sizes. Strain relaxation up to 85% of the value for the corresponding planar films can be obtained for a squared patch 100 μm in size. Finally, the enhanced thermal strain relaxation is analytically explained in terms of the Si pillar lateral tilting, critically dependent on the pillar aspect ratio, very similarly to the well-known case of a deflected beam. Our results are transferable to any material deposited, or wafer bonded at high temperature, on any patterned substrate: wafer bowing can be controlled by micrometric patterned features well within the present capabilities of deep reactive ion etching.

KEYWORDS: stress relaxation, semiconductor material, finite elements, thermal strain, Germanium.

## 1. INTRODUCTION

Mismatch between the thermal expansion coefficients of any thick film (epitaxially crystalline, polycrystalline, or amorphous) and the underlying substrate generates a stress field and, in turn, warping or cracking of the system, as soon as it is cooled down to room temperature, after high-temperature deposition[1, 2]. While the problems related to the lattice misfit between one epitaxial layer and the substrate have been partially addressed in the recent decades, by minimizing the threading dislocation density with different strategies[3-10], the more general problem of

substantially reducing the thermal strain has not been satisfactorily solved, so far[11]. Actually, beyond the trivial observation that deposition on mesas, or in oxide windows limited in lateral size, allows for a reduction of the total elastic budget, it has been recently demonstrated that selective deposition on top of tall pillars or ridges, patterned in the substrate with high aspect ratio, minimizes the thermal strain[12-14]. This is because the vertical sidewalls allow for the elastic relaxation of thermal strain, via the well-known zeroing of the stress component normal to the free surfaces. However, this aspect ratio strategy works well for a micrometric cross-cut size of the ridges or for pillars having a lateral size smaller than the height, i.e. aspect ratio larger than 4.[12, 13] This strategy is effective also for smaller aspect ratios, namely between 1 and 0.3, provided that the deposited thickness is of few microns[14]. Unfortunately, the recent need for integrating Ge photodetectors and, particularly, SiC and GaN power devices on Si, calls for thicker films (several microns) and larger areas (up to the millimeter size). This is a challenging task if a moderate wafer warping is targeted, in order to allow further processing of the wafer.

Recently, two dimensional (2D) simulations of the GaN/Si system, based on the Finite Element Method (FEM) approach[15], have suggested that a substantial improvement in thermal stress management is accomplished when the film is deposited as a continuous patch, suspended on periodic elevated features (ridges in the two dimensional model) with sufficiently high aspect ratio (5-10). Still, no explanation of the basic mechanism providing such improvement, nor its efficiency in releasing the total strain at different patch sizes, and, more importantly, no experimental confirmation have been provided.

Here we investigate the thermal strain release in Ge patches on micrometric Si pillars, for different pillar widths and patch sizes, by combining 3D and 2D FEM simulations, epitaxial depositions on patterned Si substrates, μ-Raman, μ-Photoluminescence (μ-PL), and X-ray

diffraction (XRD) measurements. An extremely efficient thermal strain relaxation is observed in the suspended Ge layers, for patches of 100 μm in size, and is explained in terms of the Si pillar lateral tilting, critically dependent on the pillar aspect ratio, very similarly to the well know case of a deflected beam. Actually, micrometric Si pillar tilting is already used in measuring the retraction of biological cells placed on top of them under different conditions[16].

## 2. MATERIAL AND METHODS

In this work, 8 μm Ge were deposited by Low Energy Plasma Enhanced Chemical Vapor deposition (LEPECVD)[17] at 575 °C on Si substrates, previously patterned in pillars by standard optical lithography and Bosch-process etching. The error in the growth temperature is estimated to be ±5°C. Patterned substrates were cleaned, prior to epitaxial growth, by using a standard RCA cleaning followed by diluted (≈5%) HF dipping, as required to remove the silicon-oxide and leave a hydrogen-terminated surface. After the insertion in the ultra-high-vacuum deposition chamber, the substrates were out-gassed for ≈ 5 min at 300 °C.

Here, the merging of the Ge crystals was induced by 6 thermal cycles, between 600 °C and 800 °C, in situ after the deposition. The pillars are arranged in square arrays, featuring different pillar periodicity (1-4 μm), and patch size $w$ (100, 200, and 300 μm). Fully-merged layers, partially merged networks, or still individual Ge crystals can be obtained, depending on the increasing pillar distance.

Raman spectra were collected in a Jobin Yvon T64000 spectrometer (532 nm laser wavelength, 0.6 mW laser power, 100× NA=0.9 objective, 0.8 μm spot diameter). In-plane strain was estimated from spectral shifts of the Ge-Ge optical phonon Raman mode. Differences in Raman shifts were calibrated on the Ge-Ge mode of a relaxed Ge wafer and converted in strain

values using the phonon strain-shift coefficient $b^{Ge\text{-}Ge} = -440\ cm^{-1}$.[18] Line scans with 1-2 μm step size were performed on square patches, both along the diagonal and from the middle of an edge to the opposite side. For each sample the data were acquired over three different patches. The accuracy in the determination of the Raman shift was lower than $0.1\ cm^{-1}$.

The samples presented in this paper have also been investigated by means of PL measurements performed at 300 K.[19] A 532 nm wavelength laser was used to excite the sample through a NA = 0.42 objective, resulting in a 1.5 μm spot diameter and a 10 mW incident power. The μ-PL signal was collected using the same objective, dispersed by 500 mm focal length monochromator and revealed by a Peltier-cooled InGaAs detector array.

XRD analyses were performed with a SmartLab μHR diffractometer from Rigaku using Cu Kα radiation in a set-up with twofold Ge(400) channel-cut collimator and twofold Ge(220) channel-cut analyzer. The illuminated sample area is about $1\times1\ mm^2$. Omega scans were performed at fixed 2θ positions, corresponding to the Si(004) and Ge(004) reflections, respectively.

## 3. RESULTS AND DISCUSSION

As illustrated in Refs. 20 and 21, the epitaxial growth of Ge in a kinetic regime, on top of Si pillars arrays, some μm-tall, few μm-spaced, may result in the formation of self-aligned individual Ge crystals, as tall as several tens of μm. This vertical growth originates from the combined effect of the short surface diffusion length, provided by the high deposition rates (~ 4 $nm\ s^{-1}$) of LEPECVD[17] at relatively low temperatures (~ 450–550 °C), and the mutual shielding of the reactive gas flux at the sidewalls by the neighboring crystals. A typical pattern outline consists of 8 μm tall Si pillar, 2×2 or 1×1 $\mu m^2$ in base, spaced by a few μm, where the Ge

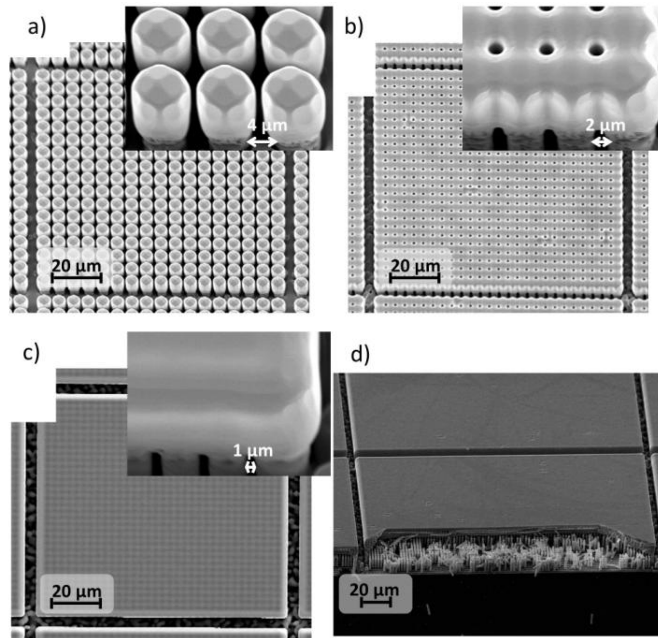


**Figure 1** SEM images of 8 μm Ge deposition, out of the same wafer, taken in different patterns: 2×2 $\mu m^2$ pillars separated by 4, 2 and 1 μm in panels (a), (b) and (c), respectively, with magnified insets, and 1×1 $\mu m^2$ pillars separated by 1 μm in panel (d).

crystals initially grow in 3D and then proceed vertically for several micrometers, separated by narrow gaps of ~50-100 nm, so that thermal strain is fully accommodated by the high aspect ratio[12, 13]. In two recent papers[22, 23], we demonstrated that, by subsequent annealing in situ, or by increasing the growth temperature during the deposition of 8 μm Ge on the pillars, full merging of the Ge crystals in a continuous and flat patch can be obtained. Obviously, this fusion results in the re-appearance of thermal strain, as the sample is cooled down at room temperature.

In Figure 1, we display the Scanning Electron Microscope (SEM) images of different arrays on the same 4" wafer: patterns composed by 2×2 $\mu m^2$ pillars separated by 4, 2, and 1 μm are reported in panels (a), (b) and (c) (with magnified insets), respectively, and 1×1 $\mu m^2$ pillars separated by 1 μm are in panel (d). In Refs. 22-24 we describe in detail the formation mechanism of such layers with one prolonged *in situ* annealing, which essentially provides the

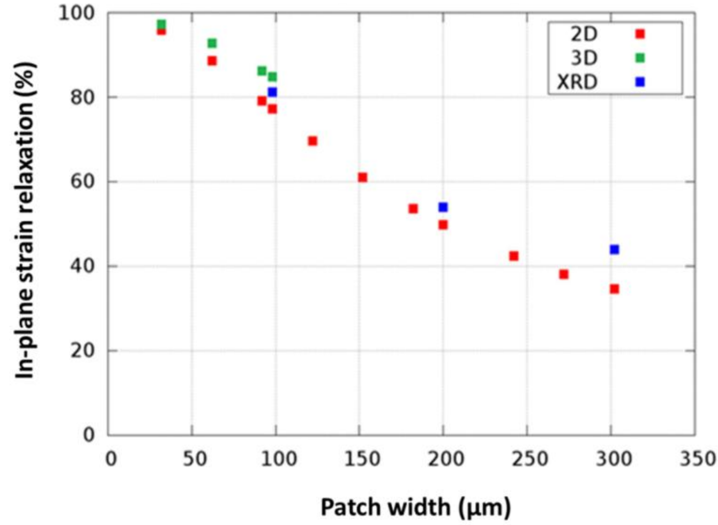


**Figure 2** Percentage of in-plane strain relaxation with respect to the unpatterned area in function of the patch dimensions as reported by 2D (red square), 3D (green square) calculation and experimental XRD measurements (blue square).

same result of the present case. Here we focus on the thermal strain relaxation in fully-merged layers (panels (c) and (d)), drawing a series of general considerations that apply independently of the nature and the microstructure of the deposited film.

If $\alpha_{epi}$ is the thermal expansion coefficient of the epilayer, $\alpha_{sub}$ the one of the substrate, and $T_{dep}$ the deposition temperature for a planar wafer, where the lattice misfit is fully accommodated by dislocations, a thermal strain

$$\varepsilon_{therm} = \int_{T_{room}}^{T_{dep}} [\alpha_{epi}(T) - \alpha_{sub}(T)]\, dT \qquad (1)$$

is accumulated during the cooling down to room temperature ($T_{room}$). Taking known values of the thermal expansion coefficients as 5.9×10$^{-6}$ °C$^{-1}$ for the Ge epilayer and as 2.6×10$^{-6}$ °C$^{-1}$ for the Si substrate, together with $T_{dep}$ = 575°C, yields an expected tensile strain of $\varepsilon_{therm}$=1.85×10$^{-3}$. However, a partial compensation with the residual compressive strain due to the hardening limit of Ge has to be expected[25]. Indeed, X-ray measurements on the unpatterned region of our

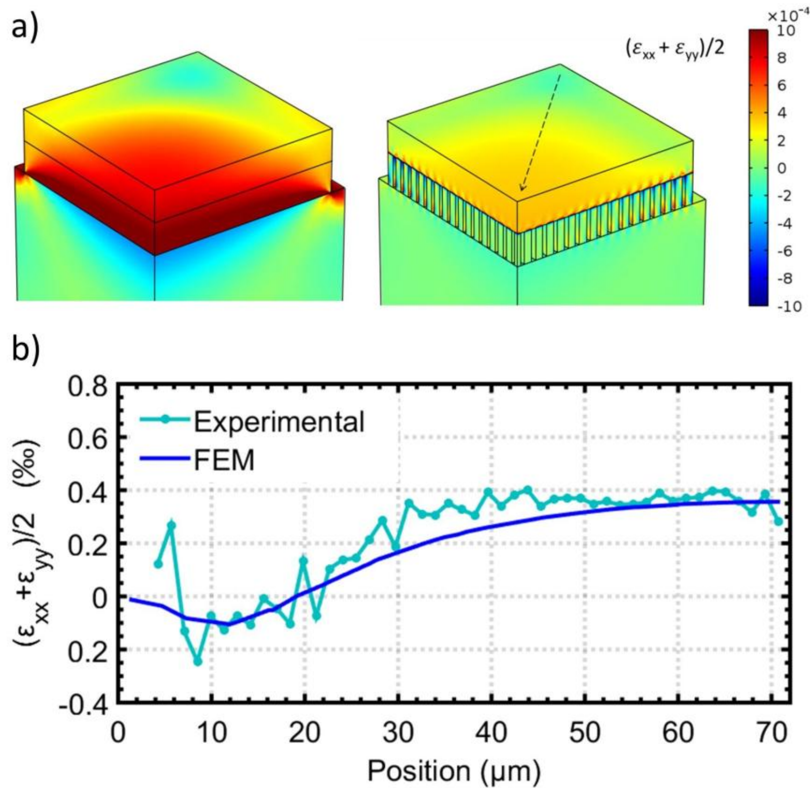


**Figure 3** a) Comparison of the residual in-plane strain values in a quarter of a 100 μm full mesa and the corresponding patch, suspended on 2×2 μm$^2$ pillars, as obtained by 3D FEM simulations. b) Comparison between simulations and μ-Raman measurements of the average in-plane strain along the diagonal of the patch [black arrow in a)] Error bars for the Raman measurements are reported and discussed in the Supplementary Material.

samples provided $\varepsilon_{therm} = 1.65\times10^{-3}$, a value also taken as the initial reference in our simulations on the compliant substrate. Actually, for suspended Ge patches very large in lateral size, the strain should be equal to the one in the unpatterned region, but for some edge relaxation.

FEM simulations by Comsol Multiphysics package have been performed for all the different patches, where the Si substrate is thick as 1 mm with a rigid constraint in the bottom part. Fully 3D configurations have been considered for the smaller patches (100 $\mu$m in *w* and 150 μm-thick substrates), whereas 2D calculations, corresponding to a central crosscut of the patch, have been performed in the remaining cases, because of computational limits. However, the relevant information is the same: in Figure 2 we report the percentage of total in-plane strain relaxation

with respect to the unpatterned area, as obtained with 2D, 3D calculation and XRD measurements. It is understood that the latter ones lie between 3D and 2D calculations, the difference being only of few percent. For example, the strain relaxation in the 100 µm patch is 81% from XRD, while the 2D prediction is 78% and the 3D one is 85%.

In Figure 3 panel (a), we compare the color maps of the site-dependent in-plane strain ($\varepsilon_{in-plane} = (\varepsilon_{xx} + \varepsilon_{yy})/2$) for one monolithic Si mesa (8 $\mu$m in thickness) with 8 $\mu$m Ge on top (left), and the corresponding suspended patch with 2×2 $\mu m^2$ pillars below (right), both for $w$=100 $\mu$m. For symmetry reasons only one quarter of the full patch is displayed. We see that the thermal strain relaxation is predicted to be much larger in the second case, particularly at the center of the patch, where the residual strain value is $\varepsilon_{therm} = 4\times10^{-4}$, while at the mesa center it remains $\varepsilon_{therm} = 1.65\times10^{-3}$ in agreement with the experimental value. As stated above, the strain reduction for the whole Ge layer due to the pillar pattern equals 85% with respect to the film deposited onto a continuous substrate. Notice that, by calculating the radius of curvature for such a residual strain with a 1 mm flexible substrate[25] and comparing it to the one for the unpatterned Si substrate with 8 $\mu$m Ge on top, the radius decreases from 107 to 16 meters.

In Figure 3 b) the calculated in-plane strain variation at the surface across half of the diagonal of the squared patch, as large as 100 µm, starting from the corner, is compared to the one measured by $\mu$-Raman spectroscopy.

Actually, comparison to the FEM prediction provides an excellent agreement, but for the data at the corner. In that portion, the Ge material is understood to have some small intermixing process with Si atoms coming from the unmasked substrate (less than 5%, probably limited to a

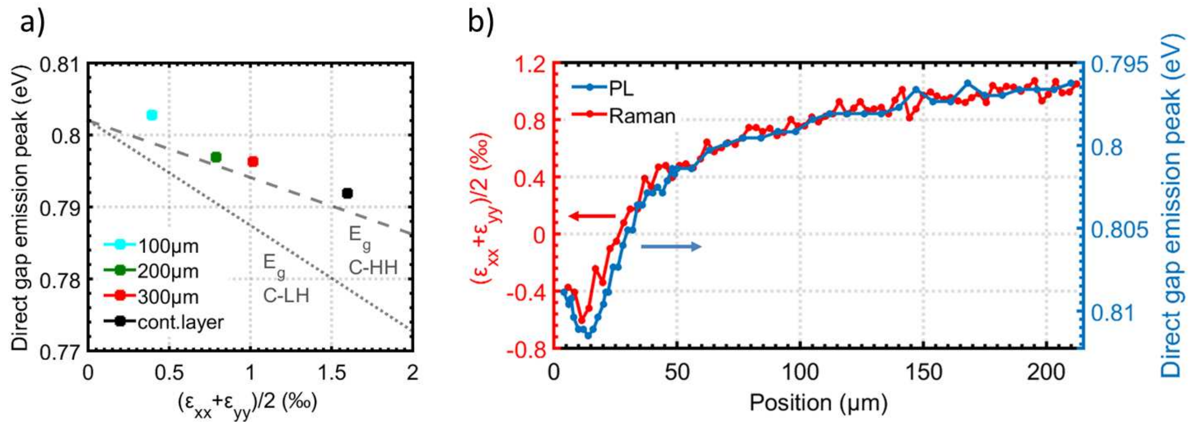


**Figure 4** a) Energy position of the direct gap emission peak measured at the center of 100, 200 and 300 µm patches and of a continuous Ge layer as a function of biaxial in-plane tensile strain values obtained from Raman data. The comparison highlights the strain dependence of the direct gap recombination involving light (C-LH) and the heavy (C-HH) hole states. b) Comparison between the biaxial in-plane strain values derived from Raman measurements and the room temperature photoluminescence peak positions obtained by moving from the corner to the center of a 300 µm side patch. The two y axes have been offset to get the same value at the center of the patch and rescaled according to the corresponding deformation potentials inferred from panel a).

thin superficial layer), so that the strain values estimated from the Raman signal have a larger uncertainty (a quantitative discussion of the effect of intermixing on Raman data and the accuracy of the strain determination is reported in the Supplementary Material). In order to confirm our quantitative estimation, the samples have been investigated also by PL. The direct gap emission comprises the radiative recombination involving conduction band electrons (C) and strain split light (LH) and heavy (HH) holes[26]. Even though at room temperature these two contributions cannot be spectrally resolved, the PL peak positions show a HH-like character[27] and follows the expected linear dependence upon the in-plane biaxial strain[28] (see Figure 4a).

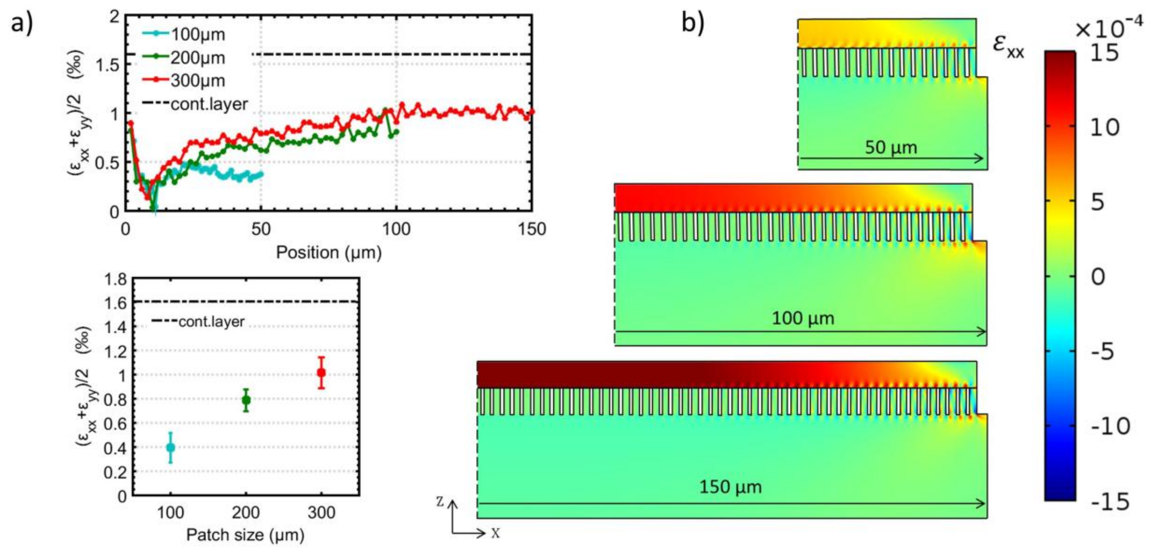


**Figure 5** a) Strain relaxation in 100, 200 and 300 µm patches as measured by µ-Raman: the trend from the edge to the center (top graph) and the values taken at the center (bottom graph). b) Color maps of the in-plane strain along a central cross-cut for the three patches, as resulting by simulations for any patch sizes.

Figure 4b shows a very good agreement between the PL and the intermixing-corrected Raman data describing the thermal strain variation across half of the diagonal of a patch of 300 µm in side, starting from the corner and moving towards the center. This comparison offers additional evidence supporting the validity of the correction for the Si intermixing effect. Moreover, since PL measurements are not affected by the presence of Si and the signal is collected from a more than 2 µm thick region, much deeper than Raman penetration length, the alloying is probably limited to a thin top layer. A reasonable explanation is that surface diffusion of Si atoms from the unmasked substrate takes place during the thermal cycles performed at the end of the growth process.

When moving to larger patches (Figure 5a, top panel), the $\mu$-Raman scans from the middle of one edge to the center of the patch indicate that the residual strain at the center is higher, but still well below the value for a mesa, or for a continuous Ge film on a flat Si substrate (dot-dashed

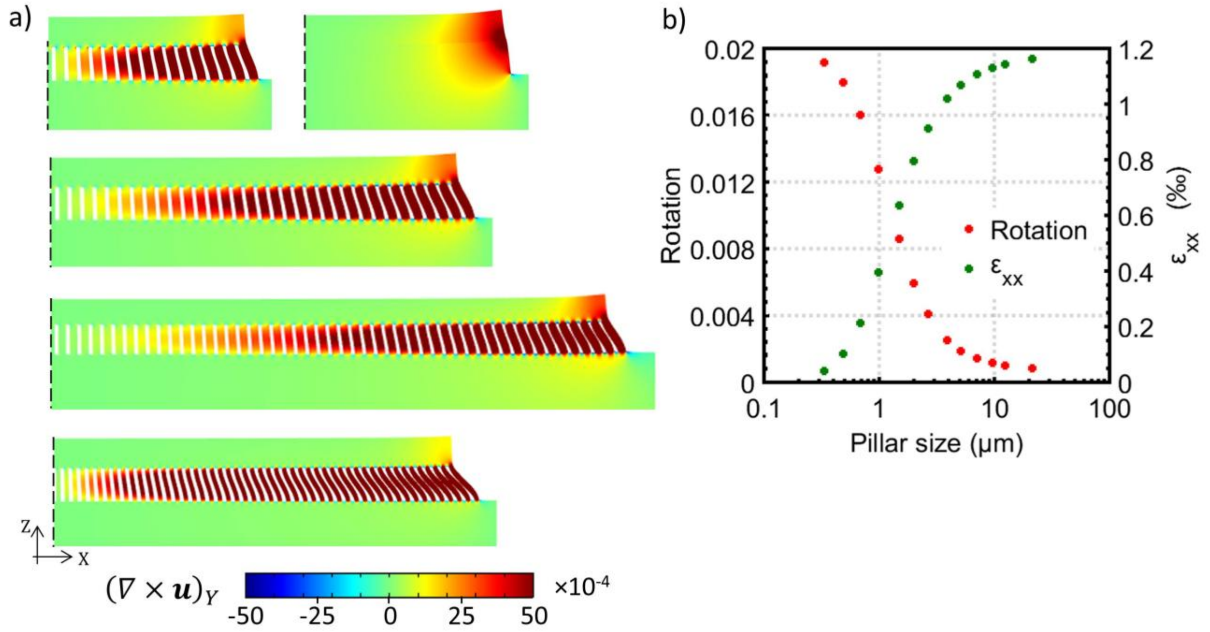


**Figure 6** a) Color maps of the rotational tensor component relative to the tilt around the y axis perpendicular to the images as obtained in 2D simulations. The structures are plotted in the deformed geometries resulting from the relaxation (magnified by a factor 55). b) FEM results of the average pillar rotation in a 200 µm patch and the relative residual strain in the Ge layer for different pillar bases.

line), and that the maximum value increases slightly sub-linearly with the patch size (Figure 5a, bottom panel). This trend is well reproduced by the simulated in-plane strain maps at the central crosscut of the patches (Figure 5b). Actually, the highly relaxed region close to the edge shows the same intensity and comparable extension for different patch sizes, independently of the fact that the contraction force should be larger for larger patches: this calls for a mechanism rather different from the material deformation acting in bulk mesas.

By FEM simulations it is possible to extract the Jacobian tensor of the displacements, $u_i$, defined as

$$\hat{J}_{ij} = \{J_{ij}, \quad i, j = 1,2,3\} \quad J_{ij} = \frac{\partial u_i}{\partial x_j} \tag{2}$$

which, in turn, is decomposed into the strain component $\varepsilon_{ij}$ (entering the strain energy) and the purely rotational component $\Omega_{ij}$ (not contributing to strain energy):

$$J_{ij} = \frac{1}{2}\left(\frac{\partial u_i}{\partial x_j} + \frac{\partial u_j}{\partial x_i}\right) + \frac{1}{2}\left(\frac{\partial u_i}{\partial x_j} - \frac{\partial u_j}{\partial x_i}\right) = \varepsilon_{ij} + \Omega_{ij} \qquad (3)$$

In panel (a) of Figure 6 we draw the central cross-section (only half of it is displayed, for symmetry reasons) of the different patches and the smaller mesa, along with the Si substrate, according to the magnified displacements (by a factor 55) with respect to the initial positions. A color mapping of the rotational component $\Omega_{xz} = (\nabla \times \mathrm{u})_y$, i.e. rotations around the $y$ axis perpendicular to the figure plane ([110] direction) is also reported. Notably no preferred handedness is associated to the rotation, owning to the thermal retraction of the Ge film. The tilting of the Si pillars is clear, particularly at the patch edges, where for larger patches (larger contraction force) the free rotation is larger (not fully visible because of color saturation), smoothly decreasing deep in the center of the patch. This is the essence of the enhanced compliance, which is fully appreciated when comparing pillar rotation to the local rotations in bulk Si mesa (top right drawing in the panel). The upward rotation of the Ge layer close to the patch edges is just a byproduct of the pillar tilting, as will be discussed in the following. If the pillar width is halved from 2 to 1 $\mu$m, as shown for the 200 $\mu$m patches (second and fourth drawing from the top in panel (a), respectively), the pillar rotation extends deeper to the center of the patch, explaining the larger compliance and the more uniform relaxation in the latter case. Therefore, the pillar aspect ratio determines the rotation, which in turn accompanies the epilayer contraction, reducing the total thermal strain. This mechanism sets in quite sharply for pillars 8 $\mu$m in height ($h$), as the size ($b$) decreases (see Figure 6 b), because the tilting of a vertical beam depends on the cubic power of the aspect ratio. The sigmoid behavior with $b$ of the average pillar

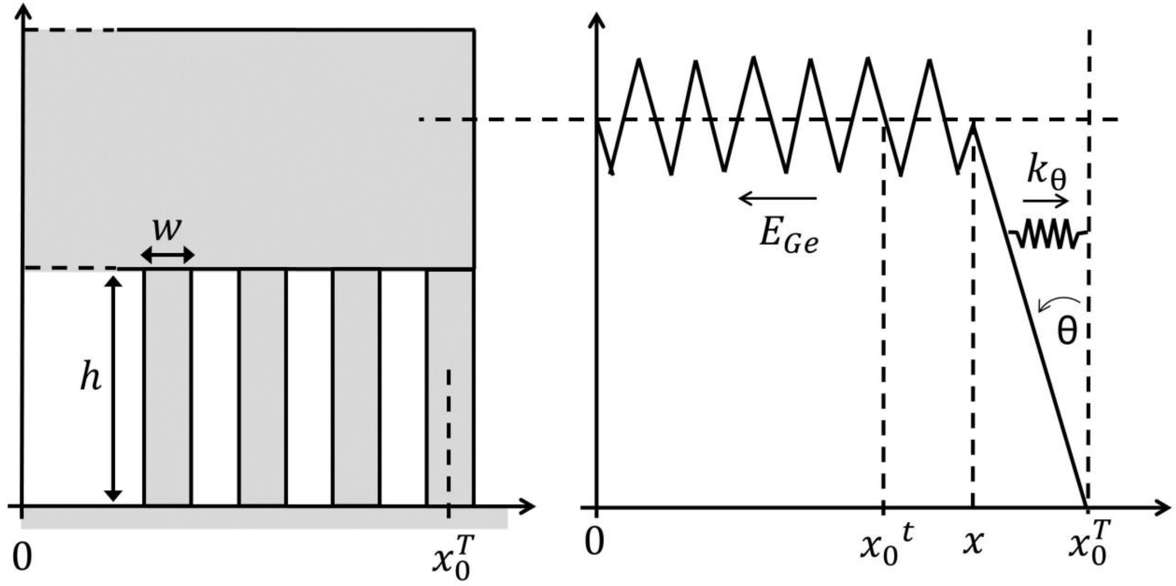


**Figure 7** Illustration defining the parameters used in the presented model. On the left the structure geometry at high temperature, on the right the structure at room temperature represented as deformed springs.

rotation for the $w$ = 100 μm patch is reported, along with the correspondingly reversed shape of the residual strain in the Ge, which is produced by the fact that, as the tilt increases with smaller $b$, the relaxation is larger and the tensile force gets smaller.

These issues are easily explained by a simple spring model of the pillar rotation ($\theta$) and the layer relaxation ($\varepsilon$) vs. $b$, as sketched in Fig. 7.

On the left panel we illustrate the patch geometry close to the right edge, as it is at the deposition temperature: null pillar rotation and full plastic relaxation of the epitaxial misfit strain in the Ge layer. Let us call $x_0^T$ the horizontal position of a generic pillar top in the array at such high temperature. When the sample is cooled at the room temperature, the Ge layer contracts, resulting in tensile stress, while the pillar rotates (Figure 7, right panel). We can define $x_0^t$ as the pillar top position that allows the full relaxation of the thermal strain in the epilayer. The

horizontal position of the pillar top $x$ results from the equilibrium between two forces: the Si pillar reaction force ($F_p$) directed towards $x_0^T$ and the contraction force ($F_{therm}$) acting in the epilayer due to the thermal stress, directed towards $x_0^t$. Defining the angles $\theta$ and $\theta_0$ as $\theta = \frac{x - x_0^T}{h}$ and $\theta_0 = \frac{x_0^t - x_0^T}{h}$, the forces can be obtained in a linear approximation. Indeed, the first term is

$$F_p = -k_\theta \left( x - x_0^T \right) = -k_\theta h \theta \tag{4}$$

where $k_\theta = E_{Si} (b/h)^3 = E_{Si} r^3$ the rotational stiffness for the Si pillar, $E_{Si}$ the silicon Young modulus and $r = b/h$ is the aspect ratio. The second force can be written as

$$F_{therm} = -E_{Ge} \left( x - x_0^t \right) = -E_{Ge} \left( x - x_0^T + x_0^T - x_0^t \right) = -E_{Ge} h (\theta - \theta_0) \tag{5}$$

where $E_{Ge}$ is the Ge Young modulus. Therefore, the balance between the two forces gives

$$-k_\theta h \theta - E_{Ge} h (\theta - \theta_0) = 0 \tag{6}$$

$$\left( k_\theta + E_{Ge} \right) \theta - E_{Ge} \theta_0 = 0 \tag{7}$$

$$\theta = \frac{E_{Ge}}{k_\theta + E_{Ge}} \theta_0 = \frac{1}{\frac{E_{Si}}{E_{Ge}} r^3 + 1} \theta_0 = \frac{1}{\chi r^3 + 1} \theta_0 \tag{8}$$

where $\chi = E_{Si} / E_{Ge}$.

Using the definition of the full thermal strain as $\varepsilon_{therm} = \frac{x_0^t - x_0^T}{x_0^t}$ we can write the residual strain in the Ge layer with compliance substrate as

$$\varepsilon = \frac{x - x_0^t}{x_0^t} = \frac{h}{x_0^t} (\theta - \theta_0) = -\frac{h}{x_0^t} \left( 1 - \frac{1}{\chi r^3 + 1} \right) \theta_0 = \frac{\chi r^3}{\chi r^3 + 1} \frac{h}{x_0^t} \frac{x_0^t - x_0^T}{h} = \frac{\chi r^3}{\chi r^3 + 1} \varepsilon_{therm} \tag{9}$$

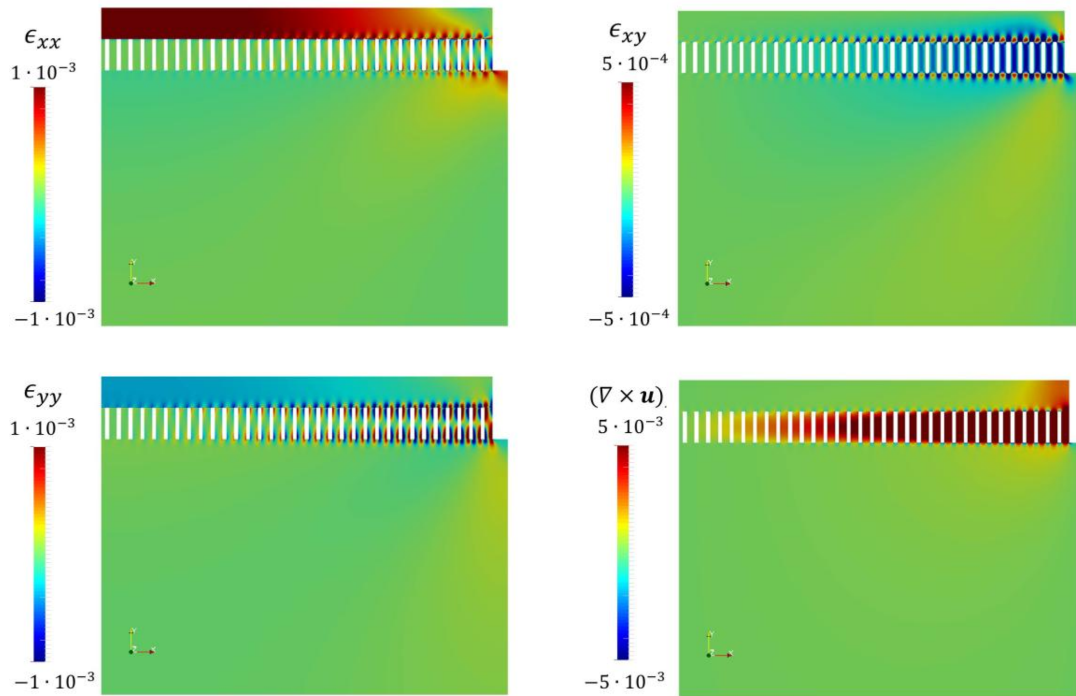


**Figure 8** Color maps of the strain and rotational tensor components as obtained by the 2-dimensional finite element method (FEM) simulations. The latter is relative to the tilt around the y axis.

Plotting in logarithmic scale $\varepsilon$ and $\theta$ vs $b$, with the small r values as the ones corresponding to the actual aspect ratios used in this work (4 and 8), the sigmoid behavior of the two curves shown in Figure 6 panel b can be perfectly reproduced. This simple analysis applies to the edge portion of any patch, and to the average rotation of the pillars in the case of small patches, where the pillar tilting nearly accommodate the full Ge contraction along the whole patch, as we will see below. In Fig. 8, we finally report, in the case of patches as large as 200 μm, the maps for the most important strain components and the rotation angle, along a central crosscut of half of the patch. Here we see that the pillar rotation does not produce a too high shear strain component (xy), and that a vertical compression/elongation is present in any tilted pillar affected by the rotation. Notably, such a small thermal strain, albeit localized, is not expected to lead to the nucleation of additional defects in the Ge film.

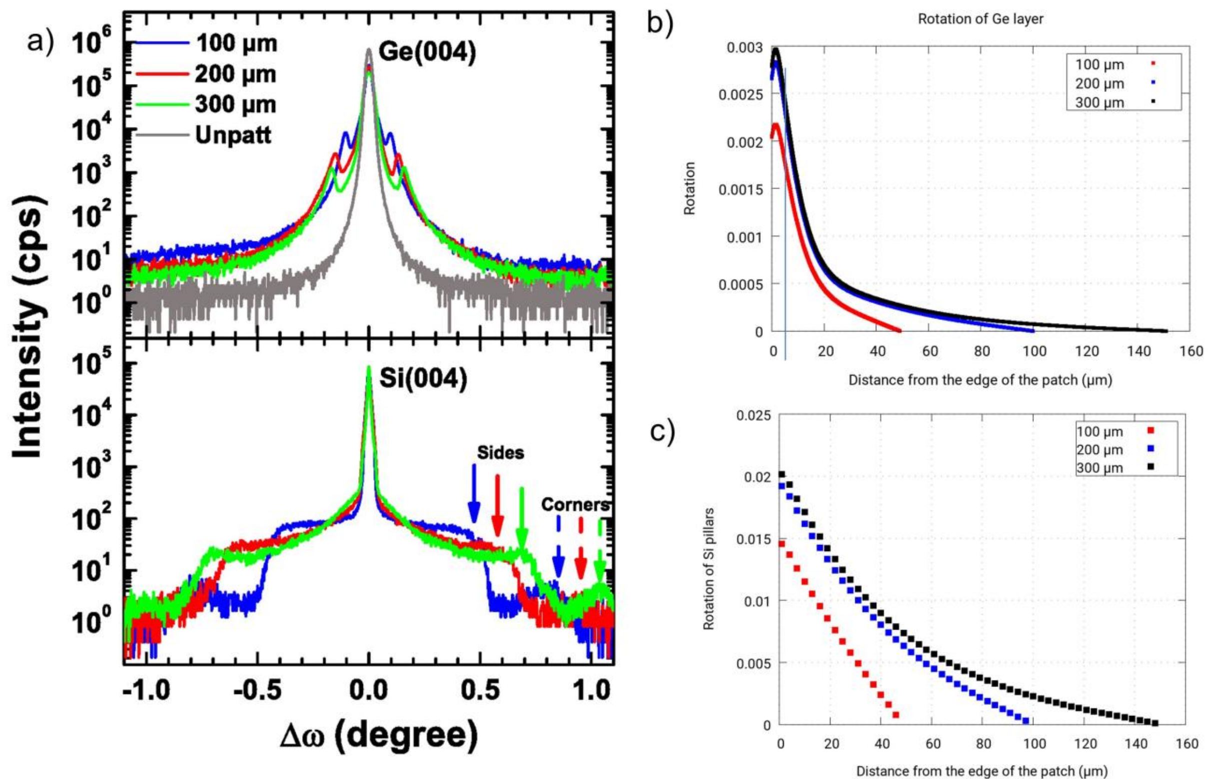


**Figure 9** a) Ge and Si tilt analysis as obtained by X-rays (004) omega scans. The rotation of the Ge layer, b), and the Si pillars, c), reported as a function of the distance from the edge of the patches having a lateral size of 100 (red squares), 200 (blue squares) and 300 (black squares) µm

As mentioned before, a well-defined portion at the edge of the Ge layer is also upward rotated (red corner in Figure 6 a). Notice that the extension of that region is the same for all the patch sizes with the same pillar aspect ratio, while the extension of the peripheral pillar rotation is somehow proportional to the patch size. Experimental data on Ge layer and Si pillar rotations have been obtained by XRD micro-focused analysis that allows us to take data in each different patch.

As we can see in the top panel a) of Figure 9, the Ge (004) omega scans show a central peak from the un-tilted central part of the Ge blocks with peaks appearing at its side, where their intensity is decreasing as the perimeter/area ratio of the different patches. This corresponds to a constant width of the peripheral tilted region, independently of the patch size, as confirmed

quantitatively by the FEM simulations in panel b) of Fig. 9. Therefore, we attribute the peaks to the tilting of the Ge layer close the patch edges. In particular, for the case of 100 $\mu$m patches, where 3D simulations have been performed, the maximum angle value obtained along the Ge patch edge is 0.090°, perfectly corresponding to the ω-scan value of 0.091°. In this case, the average residual strain in the whole Ge volume amounts to $2.4\times10^{-4}$, one order of magnitude smaller than the one for the unpatterned substrate.

The XRD signal coming from Si (Figure 9 a, lower panel) is even more interesting, because it proves the predicted symmetric tilt, acting at the two sides of the patch. Except for the central peak, coming from the unrotated Si regions, we observe a continuous tilt distribution extending to larger angles for larger patches. Such distributions are broad for any patch because the pillar rotation progressively decreases from the edge to the center of the patch as pointed out by the results of our simulations in panel c) of Figure 9. Indeed XRD shows two symmetric shoulders and additional smaller and broader peaks at larger ω angles. The former ones can be interpreted as the distribution for most of the pillars, excluding those located at the corners, and the maximum tilt corresponds perfectly to the value of 3D FEM simulations for the rotation of the last pillar in a central section (0.41°, in the case of the 100 $\mu$m). For the smaller peaks, we attribute them to the group of pillars located in the area close to the corners of the patch, and the maximum value of their tilt actually corresponds to the value found by FEM for the pillars located exactly at the patch corners (0.57°, in the case of $w$ = 100 $\mu$m).

## 4. CONCLUSIONS

In conclusion, our work, focused on the Ge/Si (001) system, shows that patterned Si substrates in pillar arrays do provide one exceptional mechanical compliance effect to the thermal strain of a

continuous Ge patch deposited on top, if the patch size is appropriate given a specific pillar aspect ratio. The micrometric dimensions and spacing of the Si pillars are within the well-established deep-etching processes, and patch sizes suitable for several applications (up to few hundreds microns) can be obtained. The sharp onset with pillar aspect ratio of such an effect is demonstrated to be triggered by the free rotation of the pillars, as induced by the thermal contraction of the film, both by FEM simulations and experimental XRD results, showing a very good quantitative agreement. Since this is a rather general mechanism, we predict it to be effective also for more demanding applications, e.g. SiC or GaN power devices, requiring thicker films and millimeter-sized patches, provided that the pillar aspect ratio is increased. Actually, preliminary simulations (to be the subject of a further publication) indicate that, in such cases, the enhanced pillar aspect ratio, necessary to keep the residual thermal strain and wafer warping within the manufacturability limits, is still accessible to standard deep-etching processes. Finally, our results provide quantitative predictions, useful for other applications, not only for electronic or photonic devices, but also in less demanding crystalline materials, such as micro-electro-mechanical systems.

ACKNOWLEDGMENT

The authors thank Dr. Roberto Bergamaschini, Dr. Marco Salvalaglio and Prof. F. Montalenti (University of Milano-Bicocca) for fruitful discussions. Support of PileGrowth Tech is gratefully acknowledged.

REFERENCES

(1) Yang, V. K.; Groenert, M.; Leitz, C. W.; Pitera, A. J.; Currie, M. T.; Fitzgerald, E. A. *J. Appl. Phys.* **2003**, 93, 3859.

(2) Sakai, M.; Egawa, T.; Hao, M.; Ishikawa, H. *Jpn. J. Appl. Phys.* **2004**, 43, 8019.

(3) Yamaguchi, M.; Yamamoto, A.; Tachikawa, M.; Itoh, Y.; Sugo, M. *Appl. Phys. Lett.* **1988**, 53, 2293.

(4) Langdo, T. A.; Leitz, C. W.; Currie, M. T.; Fitzgerald, E. A.; Lochtefeld, A.; Antoniadis, D. A. *Appl. Phys. Lett.* **2000**, 76, 3700.

(5) Fitzgerald, E. A. *J. Vac. Sci. Technol. B* **1989**, 7, 782.

(6) Paul, D. J. *Semicond. Sci. Technol.* **2004**, 19, R75.

(7) Hongdong, Y.; Qi, Y.; Xiangzhan, W.; Jingchun, L.; Ning, N.; Mohua, Y. *J. Semicond.* **2010**, 31, 063001.

(8) Ayers, J. E. *J. Electron. Mater.* **2008**, 37, 1511.

(9) Capellini, G.; De Seta, M.; Busby, Y.; Pea, M.; Evangelisti, F.; Nicotra, G.; Spinella, C.; Nardone, M.; Ferrari, C. *J. Appl. Phys.* **2010**, 107, 063504.

(10) Hoshi, Y.; Sawano, K.; Yamada, A.; Usami, N.; Arimoto, K.; Nakagawa, K.; Shiraki, Y. *J. Appl. Phys.* **2001**, 107, 103509.

(11) Giovane, L. M.; Luan, H. C.; Agarwal, A. M.; Kimerling, L. C. *Appl. Phys. Lett.* **2001**, 78, 541.

(12) Falub, C. V.; Meduna, M.; Chrastina, D.; Isa, F.; Marzegalli, A.; Kreiliger, T.; Taboada, A. G.; Isella, G.; Miglio, L.; Dommann, A.; von Känel, H. *Sci. Rep.* **2013**, 3, 2276.

(13) Meduňa, M.; Falub, C. V.; Isa, F.; Marzegalli, A.; Chrastina, D.; Isella, G.; Miglio, L.; Dommann, A.; von Känel, H. *J. Appl. Cryst.* **2016**, 49, 976-986.

(14) Gonzalez, M.; Cheng, K.; Tseng, P.; Borghs, G. Proc. of the 13th International Conference on Thermal, Mechanical and Multi-Physics Simulation and Experiments in Microelectronics and Microsystems (EuroSimE) 2012, pp. 1-6

(15) Chen, Z.; Yan, H.; Gan, Z.; Liu, S. Proc. of the 59th IEEE Electronic Components and Technology Conference 1-4 (2009) 1824.

(16) Alopan, Y.; Icoz, K.; Gurkan, U.A. *Biotech. Adv.* **2015**, 33, 1727.

(17) Rosenblad, C.; Deller, H. R.; Dommann, A.; Meyer, T.; Schroeter, P.; von Känel, H. *J. Vac. Sci. Technol. A* **1998**, 16, 2785.

(18) Pezzoli, F.; Bonera, E.; Grilli, E.; Guzzi, M.; Sanguinetti, S.; Chrastina, D.; Isella, G.; von Känel, H.; Wintersberger, E.; Stangl, J.; Bauer, G. *J. Appl. Phys.* **2008**, 103, 093521.

(19) Pezzoli, F.; Isa, F.; Isella, G.; Falub, C. V.; Kreiliger, T.; Salvalaglio, M.; Bergamaschini, R.; Grilli, E.; Guzzi, M.; von Känel, H.; Miglio, L. *Phys. Rev. Appl.* **2014**, 1, 044005.

(20) Falub, C. V.; von Känel, H.; Isa, F.; Bergamaschini, R.; Marzegalli, A.; Chrastina, D.; Isella, G.; Müller, E.; Niedermann, P.; Miglio, L. *Science* **2012**, 335, 1330.

(21) Bergamaschini, R.; Isa, F.; Falub, C. V.; Niedermann, P.; Müller, E.; Isella, G.; von Känel, H.; Miglio, L. *Surf. Sci. Rep.* **2013**, 68, 390.

(22) Salvalaglio, M.; Bergamaschini, R.; Isa, F.; Scaccabarozzi, A.; Isella, G.; Backofen, R.; Voigt, A.; Montalenti, F.; Capellini, G.; Schroeder, T.; von Känel, H.; Miglio, L. *ACS Appl. Mater. Interfaces* **2015**, 7, 19219.

(23) Bergamaschini, R.; Salvalaglio, M.; Scaccabarozzi, A.; Isa, F.; Falub, C. V.; Isella, G.; von Känel, H.; Montalenti, F.; Miglio, L. *J. Cryst. Growth* **2016**, 440, 86.

(24) Salvalaglio, M.; Bergamaschini, R.; Backofen, R.; Voigt, A.; Montalenti, F.; Miglio, L. *Appl. Surf. Sci.* **2016**, accepted. http://dx.doi.org/10.1016/j.apsusc.2016.05.075

(25) Capellini, G.; De Seta, M.; Zaumseil, P.; Kozlowski, G.; Schroeder, T. *J. Appl. Phys.* **2012**, 111, 073518.

(26) Vitiello, E.; Virgilio, M.; Giorgioni, A.; Frigerio, J.; Gatti, E.; De Cesari, S.; Bonera, E.; Grilli, E.; Isella, G.; Pezzoli, F. *Phys. Rev. B* **2015**, 92, 201203(R).

(27) Boztug, C.; Sanchez-Perez, J. R.; Cavallo, F.; Lagally, M. G.; Paiella, R. *ACS Nano* **2014**, 8, 3136.

(28) Ishikawa, Y.; Wada, K.; Liu, J.; Cannon, D. D.; Luan, H. C.; Michel, J.; Kimerling, L. C. *J. Appl. Phys.* **2005**, 98, 013501.